Imprinting isolated single iron atoms onto mesoporous silica by templating with metallosurfactants

Y. Berro, S. Gueddida, Y. Bouizi, C. Bellouard, El-E. Bendeif, A. Gansmuller, A. Celzard, V. Fierro, D. Ihiawakrim, O. Ersen, et al.

Imprinting isolated single iron atoms onto mesoporous silica by templating with metallosurfactants

Y. Berro,[1,2,3] S. Gueddida,[2] Y. Bouizi,[1] C. Bellouard,[4,*] El-E. Bendeif,[5] A. Gansmuller,[5] A. Celzard,[6] V. Fierro,[6] D. Ihiawakrim,[7] O. Ersen,[7] M. Kassir,[3] F. El Haj Hassan,[3] S. Lebegue,[2] M. Badawi,[2] N. Canilho,[1] and A. Pasc[1,*]

[1] L2CM UMR CNRS 7053, Université de Lorraine, 54506 Vandœuvre-lès-Nancy, France

[2] LPCT UMR CNRS 7019, Université de Lorraine, 54506, Vandœuvre-lès-Nancy, France

[3] PRASE, Université Libanaise, Hadath, Lebanon

[4] IJL UMR CNRS 7198, Université de Lorraine, 54000 Nancy, France

[5] CRM2 UMR CNRS 7036, Université de Lorraine, 54506 Vandœuvre-lès-Nancy, France

[6] IJL UMR CNRS 7198, Université de Lorraine, 88000 Epinal, France

[7] IPCMS UMR CNRS 7504, Université de Strasbourg, 67034 Strasbourg, France

Corresponding author: **christine.bellouard@univ-lorraine.fr, andreea.pasc@univ-lorraine.fr**

Abstract

Hypothesis

One of the main drawbacks of metal-supported materials, traditionally prepared by the impregnation of metal salts onto pre-synthesized porous supports, is the formation of large and unevenly dispersed particles. Generally, the larger are the particles, the lower is the number of catalytic sites. Maximum atom exposure can be reached within single-atom materials, which appear therefore as the next generation of porous catalysts.

Experiments

Herein, we designed single iron atom-supported silica materials through sol-gel hydrothermal treatment using mixtures of a non-ionic surfactant (Pluronic P123) and a metallosurfactant (cetyltrimethylammoniumtrichloromonobromoferrate, CTAF) as porogens. The ratio between the Pluronic P123 and the CTAF enables to control the silica structural and textural properties. More importantly, CTAF acts as an iron source, which amount could be simply tuned by varying the non-ionic/metallo surfactants molar ratio.

Findings

The fine distribution of iron atoms onto the silica mesopores results from the iron distribution within the mixed micelles, which serve as templates for the polymerization of the silica matrix. Several characterization methods were used to determine the structural and textural properties of the silica material (XRD, N_2 sorption isotherms and TEM) and the homogeneous distribution and lack of clustering of iron atoms in the resulting materials (elemental analysis, magnetic measurements, pair distribution function (PDF), MAS-NMR and TEM mapping). The oxidation and spin state of single-iron atoms determined from their magnetic properties were confirmed by DFT calculations. This strategy might find straightforward applications in preparing versatile single atom catalysts, with improved efficiency compared to nanosized ones.

Graphical abstract

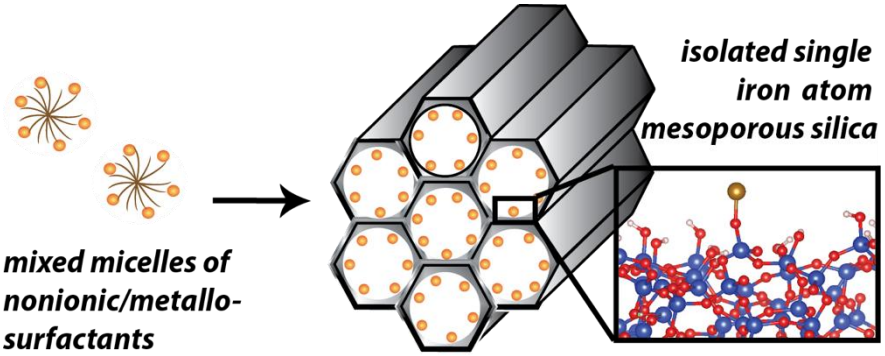

Keywords:

Single iron atom catalysts, mesoporous silica, metallosurfactants, Density Functional Theory, spin state, pair distribution function.

1. Introduction

Increasing the number of active sites of a material in order to enhance its catalytic activity is a continuous challenge [1–3]. This is commonly addressed by increasing the active surface area of catalytic particles and thus by decreasing their size. The most promising catalysts with the lowest size limit and thus, the highest atom efficiency are considered isolated single atom catalysts (SACs) [4–10]. Several studies already demonstrated the efficiency of SACs compared to nanosized catalysts. For instance, in the water gas shift reaction [11] catalyzed by Ir_1/FeO_x, single atoms promoted more

than 70% of the catalytic activity, while subnano clusters and nanoparticles accounted for less than 30%. Pt-based SAC also proved to have high activity for the CO oxidation reaction [12,13]. This was correlated with the existence of vacant 5d orbitals of Pt ions, which reduce both the CO adsorption energy and the reaction activation barriers [13,14]. Also Au-based SAC dispersed on FeO_x nanocrystallites showed higher stability and sintering resistance compared to conventional Au nanostructures [15,16]. Liu *et al.* [17] succeeded to synthetize Pd/TiO_2 SACs, having nine times higher activity for C=C bond hydrogenation reaction than commercial Pd catalysts.

The main advancement of the SAC strategy was to reach similar or better catalytic activity with non-precious metal catalysts compared to expensive noble metals [18–22]. Thus, Pt catalysts could be replaced by Co[18] or Fe[19]-based SACs in the oxygen reduction reaction (ORR). The latter actually outperformed all ORR's reported catalysts to date, including commercial Pt/C.

Despite the progress in this topic, one important challenge remaining is the preparation of SACs, with a tuned porosity and a controlled metal loading, while preventing agglomeration and migration of isolated atoms [17,23]. In 2002, Tilley *et al.* [24] proposed a new strategy for the preparation of single-site iron (III) centers, through grafting reactions of iron complex with pre-synthesized SBA-15, and proved their high selectivities as catalysts for oxidation of alkanes, alkenes, and arenes. More recently, Hock *et al.* [25] compared the catalytic performance for selective propane dehydrogenation of isolated Fe(II) synthesized via grafting on silica, iron oxide particles, and metallic nanoparticles. Herein, we show for the first time that micelles of ferrosurfactants can act as both porogen of the silica framework and as fine imprinters of iron atoms at the surface of mesopores, leading thus to the formation of mesoporous silica-supported isolated single iron atom catalysts (Fe/SiO_2 SACs) via direct one-step method. The interest in such catalysts comes from their wide applications as bifunctional metal-acidic catalysts for biomass upgrading [26], syngas production [27], Fisher-Tropsch synthesis [28–30], Friedel-Craft alkylation [31], or oxidation reactions [24,32–34].

Common synthesis methods of $Fe@SiO_2$ involve either the salt impregnation of a pre-synthesized silica support with an iron salt solution [35] or the co-precipitation method [36]. However, those routes suffer from the formation of large nanoparticles aggregates

and the interference of metal precursors during the polycondensation of the silica framework. Campelo *et al.* [37] compared different synthesis methods and showed that the co-precipitation of silica and metal precursors directed by hydrothermal sol-gel synthesis gives a better dispersion of metal species on the silica surface than the salt impregnation of a pre-synthesized silica support. However, the metal precursors interfere with the polycondensation of the silica framework, resulting in undesirable altered structural morphology [38]. Improvement of nanoparticles distribution in a mesoporous silica matrix could be reached by using self-assembled surfactant phases, such as micelles or liquid crystals [39–41]. Among them, our group reported ferrosurfactants which are able to form either micelles [42], vesicles [43] or to stabilize solid lipid nanoparticles. The latter, dispersed in a micellar solution of a non-ionic surfactant, P123, could lead to highly dispersed iron oxide nanoparticles within a mesoporous-macroporous silica matrix. The ferrosurfactant acted as the only source of iron and thus triggered the formation of nanoparticles within the macropores [44]. More recently, Yang *et al*. [20] also proposed a non-ionic surfactant (F127®)-assisted method for single iron atoms catalyst synthesis enabling the dispersion of iron species and therefore exhibiting a higher catalytic activity for ORR application.

Motivated by these pioneering works, the present study aims to elaborate mesoporous silica materials with supported isolated single iron atoms, Fe@silica SACs, through a sol-gel self-assembling mechanism from mixed micelles of non-ionic and metallo-surfactants. The non-ionic surfactant template (here the Pluronic P123®) was chosen to control the structural and textural properties of the silica framework (high surface-active area, pore volume, pore size) as it was demonstrated by XRD and N_2 sorption isotherms. More important, the metallosurfactant allows controlling the iron loading and the homogeneous distribution of iron atoms and lack of clustering as it was demonstrated by elemental analysis, STEM mapping, Pair Distribution Function (PDF) analysis, MAS-NMR and magnetic measurements.

2. Materials and methods

2.1. Chemicals

Tetramethylorthosilicate (TMOS), Pluronic® P123, and hexadecyltrimethylammonium bromide (CTAB) were purchased from Sigma-Aldrich. Iron(III) chloride ($FeCl_3$) was

purchased from Alfa Aesar. All reagents were used without further purification. Cetylrimethylammoniumtrichloromonobromoferrate (CTAF, $C_{16}H_{33}N(CH_3)^{3+}$, $FeCl_3Br^-$) was synthesized as previously reported [42–44].

2.2. Preparation of silica materials

Silica materials were prepared by sol-gel process, through the cooperative templating mechanism, from micellar solutions of P123 (M_w = 5800 g·mol^{-1}) and CTAF (M_w = 465.55 g·mol^{-1}), and TMOS (M_w = 152.22 g·mol^{-1}) as inorganic precursor. The micellar solutions were prepared by adding 200 mg of P123 and an appropriate amount of CTAF (18, 36, 90, 181 mg) in 10 mL of 1M HCl, to reach the CTAF/P123 molar ratio r of 1, 2, 5 and 10, respectively. In a typical procedure, 310 mg of TMOS were added to those micellar solutions to obtain a P123/TMOS molar ratio of 0.017. The mixture was stirred at room temperature for 30 min before being transferred into a Teflon bottle and placed in a stainless-steel autoclave at 373 K for 48 h. The resulting hybrid product was then filtered through a paper filter on a funnel and dried in air for 24 h. The surfactant can be removed by Soxhlet extraction with ethanol to lead to pristine silica (P@SiO_2(r)) or by calcination, to remove the organic part and to lead to ferrisilicates (Fe@SiO_2(r)). The programming of the calcination procedure was set as follows: (step 1) increasing temperature from room temperature (RT) to 373 K (2K·min^{-1}) and held for 1 h; (step 2) heating ramp from 373 K to 623 K (2K·min^{-1}) and held for 1 h; and (step 3) heating ramp from 623 K to 823 K (2K·min^{-1}) and held for 3 h. The yield of the sol-gel process was 80% while the one of the iron loading in ferrisilicates was evaluated to 25%, except for Fe@SiO_2(10), only 7%.

2.3. Characterization methods

2.3.1. Nitrogen sorption measurements

The textural properties of the synthesized materials after calcination were determined from the nitrogen adsorption/desorption isotherms obtained at 77 K (p/p_0 increasing from 10^{-7} to 0.99 and decreasing from 0.99 to 0.10) using an automatic Micromeritics ASAP 2020 instrument. The specific surface area was determined using two methods, the BET method[45,46] and the NLDFT method [47]. The total pore volume was determined from the nitrogen adsorption at a relative pressure of 0.97, while the meso-pore volume V_{meso} was calculated by the difference between the total pore volume and the micro-pore volume calculated using the NLDFT method. The pores size

distributions in the mesopore range were determined by the Barret–Joyner–Halenda (BJH) method with the Kruk–Jaroniec–Sayari (KJS) correction to the desorption branch of the nitrogen isotherms [48,49]. Pore diameters corresponding to peaks in the latter PSDs were labelled D_{BJH}.

2.3.2. X-ray diffraction

The measurements were performed using a Panalytical X'Pert Pro diffractometer equipped with a Cu tube, a Ge (111) incident-beam monochromator (λ=1.5406Å) and an X'Celerator detector. Small-angle X-ray scattering (SAXS) measurements were collected using 0.02 rad Soller slits, 1/16° fixed divergence and anti-scatter slits. The X'Celerator detector was used as "scanning line detector (1D)" with 0.518° active length. Data collection was carried out in the scattering angle range 0.8–12° with a 0.0167° step over 60 min.

2.3.3. Elemental analysis

Si and Fe chemical analysis were performed using an Inductively Coupled Plasma Atomic Emis-sion Spectroscopy (ICP-AES).

2.3.4. Transmission electron microscopy and element mapping

Transmission electron microscopy (TEM) analyses were performed using a JEOL 2100 F electron microscope operating at 200 kV and equipped with a probe Cs corrector. The "HAADF-STEM" images were acquired in scanning TEM (STEM) using a high angle annular dark field detector (HAADF). The elemental maps were acquired by Energy Dispersive X-Ray (EDX) Spectroscopy in STEM mode using a JEOL Silicon Drift Detector (DrySD60GV: sensor size 60 mm^2) with a solid angle of approximately 0.5 sr.

2.3.5. Total scattering X-ray measurements and PDF analysis

The total scattering X-ray measurements were performed at the High energy Beamline for Buried-interface Structures and Materials Processing ID31 of the European Synchrotron Radiation Facility (ESRF). The data-sets were collected using a large area, high energy single-photon counting detector, Pilatus3 2M CdTe and a high energy monochromatic beam (68.5 keV, λ= 0.18099 Å). Sample powder was loaded into a 1 mm diameter Kapton capillary tube. The raw two-dimensional data-sets were azimuthally integrated and converted to one-dimensional intensity versus 2θ using PyFAI software package [50]. The total scattering

measurements have been carried out under the same experimental conditions for all the studied samples (Fe@SiO_2(1), Fe@SiO_2(2), Fe@SiO_2(5) and Fe@SiO_2(10)). The collected data were then corrected for experimental effects (absorption, multiple scattering, polarization, Compton scattering and Laue diffuse scattering) and the scattering signal from the air and the experimental set up was measured independently under the exact same conditions as the samples and subtracted as a background in the data reduction procedure. The data were truncated at a finite maximum value of Q_{max} = 18 $Å^{-1}$ beyond which the signal-to-noise ratio became unfavorable. All the differential experimental atomic pair distribution functions (d-PDF) were obtained by using the PDFgetX3 program [51] and following a procedure previously reported [52,53].

2.3.6. Solid-state nuclear magnetic resonance

Solid-state NMR spectra were acquired on an AVANCE III Bruker spectrometer operating at 14 T (^{1}H NMR at 600 MHz). A Bruker 4 mm MAS probe was used for the experiment with MAS frequencies of 12.5 kHz. For ^{29}Si experiments, the (rf)-field strength applied for the 90° pulse was set to 50 kHz for a duration of 5 μs. During acquisition, SPINAL-64 ^{1}H heteronuclear decoupling was applied at an rf-field strength of 80 kHz, with a pulse length of 5.8 μs [54]. Optimized saturation recovery experiments were used for T_1 relaxation measurements with a list of 13 recovery delays. For ^{29}Si experiments a recovery delay of 300s was used for accumulating 256 scans. Regarding the evolution of ^{29}Si spinning sidebands, a recovery delay of 0.5s was used for accumulating 512 scans. A recovery delay of 3s was used for all ^{1}H experiments. The ^{1}H and ^{29}Si chemical shifts were reported relative to tetramethylsilane. The DMfit program was used for spectral deconvolution [55]. Mathematica 11.2 software was used to fit the saturation-recovery T_1 relaxation curves and to perform the corresponding statistical analysis. Before NMR measurements, filled NMR rotors have been extensively dried for 72 h, at 323 K, with a turbo-molecular vacuum pump at pressure below 10^{-4} mbar.

2.3.7. Magnetic measurements

Magnetic measurements were performed with a SQUID-VSM magnetometer (from Quantum Design) used in the dc-mode. Samples were introduced in a gelatin capsule placed in a plastic straw. Both temperature (from 2K to 400 K) and field (up to 7 T) dependences of magnetization were investigated.

2.3.8. Density functional theory calculations

Periodic spin polarized density functional theory (DFT) calculations were performed using the VASP package [56] by means of the projector augmented wave (PAW) method [57]. The GGA+U [58–60] method was used for the exchange and correlation potential, in order to take into account the strong electron-electron interaction due to the iron localized d shell. The values of the parameters U and J were set to 3 eV and 0.9 eV, respectively [61]. Dispersion effects were considered by means of the DFT-D2 correction by Grimme *et al.* [62], as implemented in VASP [63].

The interaction between a single iron atom and amorphous silica-surfaces was investigated by considering three different silanol densities: 7.2, 4.6 and 3.3 OH/nm^2 [64,65]. The fully hydroxylated surface (SiO_2-7.2) was represented by a supercell containing 402 atoms, and for SiO_2-4.6 and SiO_2-3.3, 384 and 375 atoms, respectively. In all the cases, the periodically repeated slabs were separated by more than 20 Å of vacuum in the z direction. A plane-wave basis set with a kinetic energy cutoff of 450 eV was used to ensure the convergence of our calculations. Due to the large size of the supercell, only the Γ point was used to sample the Brillouin zone. The total energy converged within 10^{-6} eV. For the atomic relaxation, the single iron atom and the atoms of the first layer of the silica-surface were relaxed by nullifying the forces on the atoms with a precision of 0.03 eV/Å and the other layers were kept fixed.

3. Results and discussion

3.1. Synthesis of silica materials

Silica materials were prepared through the self-assembling mechanism (Scheme 1) by adding a silica precursor (tetramethoxylsilane, TMOS) to a mixed micellar solution of a non-ionic surfactant, the Pluronic P123, and a metallosurfactant, CTAF, at various molar ratio, r (of 1, 2, 5, 10 where $r = n_{CTAF}/n_{P123}$). All syntheses were performed at pH 1 to prevent precipitation of iron hydroxides. Therefore, the expected silica materials would be positively charged ($SiOH_2^+$) and would need a cationic porogen to drive the silica-surfactant interaction through the anionic counterion ($SiOH_2^+/FeCl_3Br^-/CTA^+$) and to favor the imprinting of iron centers into the matrix.

The hydrothermal reaction conditions are similar to the one generally used for the synthesis of SBA-15 (hydrothermal treatment under acidic catalysis, for 48 h at 373 K) [66,67]. Indeed, under these reaction conditions and in the absence of CTAF, the pristine material exhibits hexagonally ordered mesopores of around 8 nm diameter and a surface area (A_{BET}) and pore volume of 846 $m^2 \cdot g^{-1}$ and of 0.984 $cm^3 \cdot g^{-1}$, respectively, as it was determined from XRD and N_2 adsorption measurements (Figure SI1). These values are in agreement with a typical SBA-15 silica material.[67] By adding CTAF, mixed micelles are formed. This affects both the meso-structure and the textural properties of the resulting materials, as reported in Table 1.

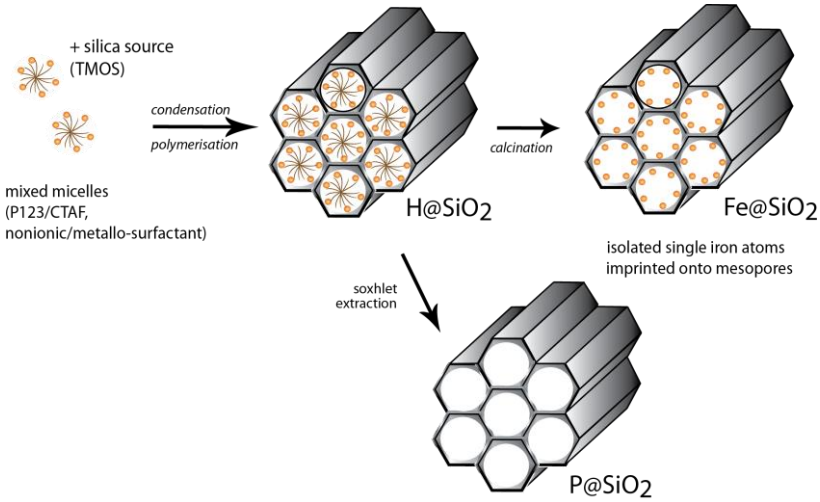

Scheme 1. Schematic representation of the sol-gel synthesis of silica materials through the self-assembling mechanism based on mixed micelles of metallosurfactant CTAF and pluronic P123.

3.2. Structural and textural characterization of Fe@SiO_2(r) materials

From the XRD data (Figure 1A), it can be first seen that the mesopore ordering of the materials decreases with the increase in CTAF content. At low r values (r= 1 and 2), the materials exhibit three reflection peaks located respectively at 9.4, 5.5 and 4.7 nm for Fe@SiO_2(1) and at 8.2, 4.9, and 4.4 nm for Fe@SiO_2(2). Their relative positions are 1, $\sqrt{3}$ and 2, which can be attributed to the (100), (110) and (200) reflections of a hexagonal structure. According to Bragg's law, the unit cell dimension (a_0) can be calculated and was found to be equal to 10.9 nm for Fe@SiO_2(1) and 9.5 nm for Fe@SiO_2(2). This decrease of the cell unit could be due to the silica wall thickness and/or pore diameter. The hexagonal ordering of the pores was further confirmed by transmission electron microscopy (TEM) micrographs showing honeycomb like arrangements (*i.e.* Fe@SiO_2(1) in Figure 2). In addition to those hexagonally organized mesopores of about 8 nm in diameter and 3 nm in

wall thickness, the micrographs also show the coexistence of larger, unorganized pores, of about 12 nm in diameter.

At higher r values (r= 5 and 10), the materials exhibit a broad peak located at 7.8 nm for Fe@SiO_2(5) and at 6.6 nm for Fe@SiO_2(10). This indicates the formation of a wormhole-like structures. The loss of ordering might be due to the increase of the total surfactant $n_{P123+CTAF}/n_{TMOS}$ molar ratio (R) with the increase of r values. As a matter of fact, in order to control the iron/silica ratio, only the P123/TMOS molar ratio was maintained constant, without adjusting R ($n_{P123+CTAF}/n_{TMOS}$) as a function of r (n_{CTAF}/n_{P123}). Yet, it is communally accepted that the parameter R is essential in getting well-defined architectures and it strongly depends on the nature of the surfactant. For instance, hexagonally ordered materials could be obtained with solely P123 at R=0.017 and with solely CTAF at R=0.17. Another important parameter influencing the morphology and the pore size of the resulting material is the size and nature of the micelles used as template. The iron ions from CTAF might induce the complexation of ethylene oxide units of P123 and thus the shrinkage of the mixed micelles and the reduction of the silica/surfactant interaction. Obviously, when increasing the CTAF content, the repetition distance decreases, indicating a decrease of the pore size and/or of the silica wall thickness.

Table 1. Textural properties of Fe@SiO_2(r) materials (r = 1, 2, 5, 10) and pristine material, obtained in the absence of CTAF: interlayer distance/unit cell dimension for hexagonal networks d_{Bragg}/a_0, pore diameter D_{BJH}, wall thickness ε, surface area A_{BET} and S_{NLDFT}, mesopores volume $V_{0.97}$, and silanols density $\rho_{Si\text{-}OH}$.

	d_{Bragg}/a_0 (nm)	D_{BJH} (nm)	ε (nm)	A_{BET} ($m^2 \cdot g^{-1}$)	S_{NLDFT} ($m^2 \cdot g^{-1}$)	$V_{0.97}$ ($cm^3 \cdot g^{-1}$)	$\rho_{Si\text{-}OH}$ (OH/nm^2)
Fe@SiO_2(1)	9.4/10.9	4.8/7.3 /12.4	3.6	731	809	1.34	9.6
Fe@SiO_2(2)	8.2/9.5	5.0/6.6 /12.3	2.9	750	819	1.41	5.5
Fe@SiO_2(5)	7.8/-	4.9	2.9	957	974	1.43	3.8
Fe@SiO_2(10)	6.6/-	5.5	1.1	993	1013	1.34	4.0
P@SiO_2	10/11.6	8	2	846	942	0.984	2.6

Further insights in the pore size distribution (PSD) were obtained from nitrogen adsorption/desorption isotherms. Except Fe@SiO_2(10), which exhibits a type IV isotherm with one hysteresis loop, characteristic of unimodal mesoporous materials, all materials rather exhibit a type II isotherms with two main steps desorption branch indicating the coexistence of mesopores of different sizes (Figure 1B). On all isotherms, it can be observed that the value of the relative pressure, at which the first capillary condensation occurs is almost the same, between 0.4 and 0.5. Since the p/p_0 position of the inflection point is related to the pore diameter, according to Kelvin's equation, this observation suggests that all materials have mesopores of about 5 nm in diameter. As a matter of fact, Fe@SiO_2(10) has a unimodal distribution of mesopores centered on 5 nm, as shown by the pore diameter distribution obtained by applying the BJH method to the nitrogen desorption isotherms (D_{BJH}, Figure 1C). The second inflection point appears for the other materials at a p/p_0 value comprised between 0.7 and 0.8, suggesting larger pores. For Fe@SiO_2(1) and Fe@SiO_2(2), three N_2 desorption steps can be identified at the following p/p_0 intervals: between 0.50 and 0.75, between 0.75 and 0.80, and between 0.80 and 0.99, which indicate the existence of mesopores within three ranges of pore diameters. For the Fe@SiO_2(5) material, one can observe two zones N_2 desorption steps, at p/p_0 between 0.50 and 0.80, corresponding to the porosity peak around 5 nm, and at p/p_0 between 0.80 and 0.99, corresponding to larger pores ($8 < D_{BJH} < 16$ nm), where $dV \cdot dD_{BJH}^{-1}$ is around 0.05 $cm^3 \cdot g^{-1} \cdot nm^{-1}$. The Fe@$SiO_2$(10) sample shows one N_2 adsorption zone ($0.50 < p/p_0 < 0.80$) corresponding to the 5 nm pore diameter peak, with no adsorption for p/p_0 above 0.80. The pore sizes of all materials are wider than the one obtained by using only CTAF as template, without adding the non-ionic P123 surfactant (of 2.4 nm).[42] So is the wall thickness, ε, as it was calculated by the subtraction of the pore size (D_{BJH}) from the interlayer distance (d_{Bragg}) for the wormlike materials and from the cell unit for the hexagonal ordered ones. The surface areas are similar for the hexagonally ordered materials Fe@SiO_2(1) and Fe@SiO_2(2) on the one hand, and for the wormlike materials Fe@SiO_2(5) and Fe@SiO_2(10) on the other hand. All materials have high surface areas, A_{BET} and S_{NLDFT}, and total pore volumes $V_{0.97}$ (Table 1). A sharp increase, of almost 200 $m^2 \cdot g^{-1}$, can be noticed between the two series of materials. Therefore, Fe@SiO_2(5) and Fe@SiO_2(10) might be considered more attractive for catalytic applications, such as in hydrodeoxygenation reactions for example.

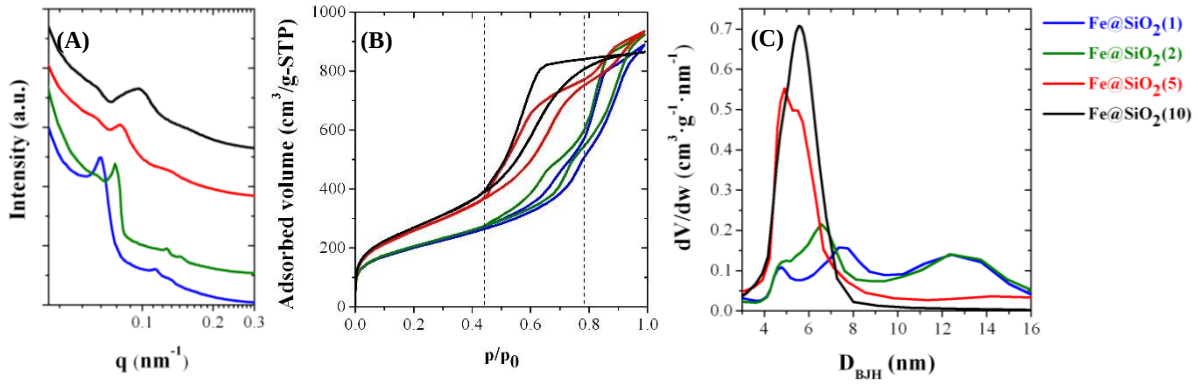

Figure 1. Textural properties of Fe@SiO_2(r) materials (r = n_{CTAF}/n_{P123} = 1, 2, 5, 10): (A) XRD patterns, (B) N_2 adsorption-desorption isotherms, and (C) pore size distribution.

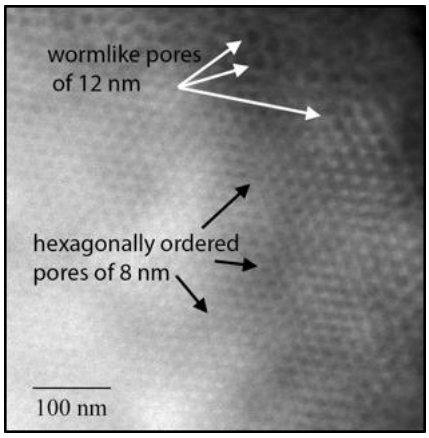

Figure 2. Transmission electron micrograph of Fe@SiO_2(1).

3.3. Chemical characterization of Fe@SiO_2(r) materials

The attenuated total reflectance infrared ATR-IR spectra of Fe@SiO2(r) materials confirms the formation of the silica framework during the sol-gel process and the removal of the organic part of the surfactant after calcination. Characteristic peaks of the stretching and bending vibrations of Si-O-Si, Si-O and Si-OH bonds are present in the 900-1100 cm^{-1} region, while no peaks of CH_2 moieties appear between 2800 and 2900 cm^{-1} (Figure SI2 left). The ATR spectra also show the presence of OH groups at 1633 cm^{-1} and at 3200-3700 cm^{-1} that were assigned to silanol groups and physisorbed water, respectively. Quantitative assessment of silanol densities on the surface of those materials was obtained from BET and TGA analysis (Table 1 and SI3 for the calculation method).

All materials exhibit silanols density values higher than for the similarly synthesized SBA-15-like silica, with no CTAF (around 2.50 OH/nm^2). This may be due to the existence of iron

atoms that hinder silica crosslinking during the polymerization, which may indicate the formation of Si-O(H)…Fe bonds instead of Si-O-Si bonds.

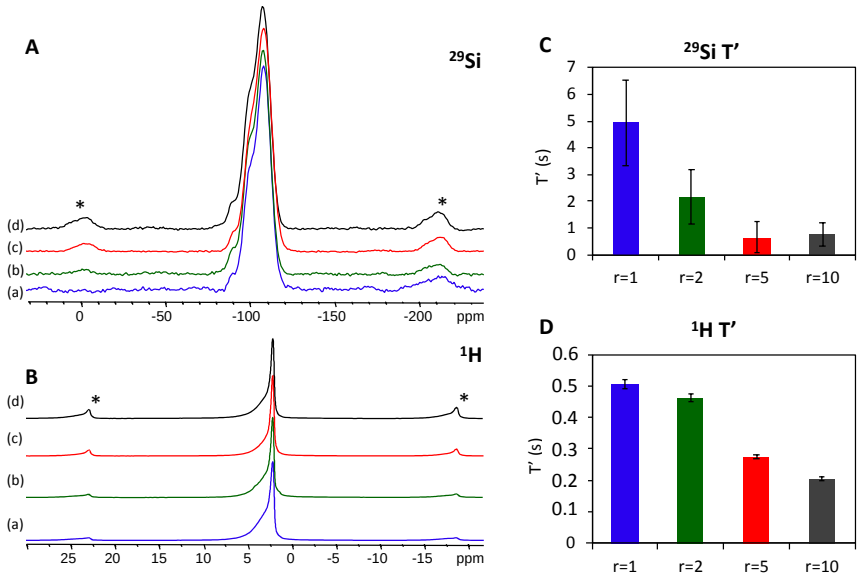

Figure 3. Evolution of ^{29}Si (A) and ^{1}H (B) MAS NMR spectra for increasing r values of Fe@SiO_2(r) materials: (a) r=1; (b) r=2; (c) r=5 and (d) r=10. Spinning sidebands are marked by * and ν^{MAS} =12.5kHz. Histograms showing the evolution of ^{29}Si (C) and ^{1}H (D) characteristic T' spin-lattice relaxation times for increasing r-values in Fe@SiO_2(r) materials. Saturation recovery curves have been fitted to "stretched exponential" functions with β=0.5 for ^{29}Si and β=0.74 for ^{1}H. Error bars reflect the 95% confidence interval of the fits.

The condensation degree of silica in Fe@SiO_2(r) materials could be assessed from ^{29}Si solid-state NMR. Relative proportions of Q_2 ($SiO_2(OH)_2$ silanols), Q_3 (SiO_3(OH) silanols), and Q_4 (SiO_4 bonds) units were determined after deconvolution of the peaks at -91, -100 and -110 ppm, respectively and all materials exhibit the same condensation degree Q_2:Q_3:Q_4 of 4:24:72 (+/-2%). Nevertheless, despite the absence of additional ^{29}Si signals, evidence is found for the presence of paramagnetic Fe. Indeed, the very high magnetic moment of unpaired electrons, located at paramagnetic centers, affects the NMR properties of coupled spins in different ways [68]. Nuclei that are chemically bound, or in the first coordination shell of paramagnetic iron cannot be observed due to extreme paramagnetic broadening. However, above this cutoff radius, nuclear spins become observable despite considerable paramagnetic broadening [69]. Under Magic Angle Spinning (MAS) sample rotation, this broadening gives rise to intense sideband patterns in the MAS NMR spectra, which are separated from the isotropic signal by multiples of the rotation frequency [70]. Since the gradual signal loss and broadening occur simultaneously, the boundary between observable and non-observable spins is somewhat

diffuse (~3.3Å) [71,72], nevertheless it is possible to distinguish between short range effects, inducing signal loss, and medium range effects up to the nanometer scale, inducing line broadening and spin lattice R_1 relaxation. Because of the low Fe concentration in the materials studied here, no short-range effects like the decrease in signal intensity or selective loss of pore surface (Q_2/Q_3) sites with Fe loading could be established. Indeed, even for Fe@SiO_2(10), the Fe content remains below 2 wt.% (Table 2). Nevertheless, medium-range effects such as an increase of sideband pattern intensity is indeed observed for ^{29}Si and ^{1}H NMR spectra when the CTAF/P123 ratio increases (Figure 3 A,B). This qualitative result is a consequence of the presence of paramagnetic species and indicates an increase of the average spatial proximity between paramagnetic iron spins and the diamagnetic neighbors, at the subnanometric scale as determined by the pair distribution function analysis (PDF).

Additionally, the study of spin lattice R_1 relaxation also shows the existence of medium-range paramagnetic effects. Indeed, the ^{29}Si and ^{1}H characteristic T_1 relaxation times are low compared to standard SBA-15 type material and therefore semi-quantitative information is best obtained by fitting the peak areas (M) obtained from saturation recovery experiments to a modified "stretched exponential" equation of characteristic time T' with $\beta < 1$.

$$\frac{M}{M_\infty} = a\,(1 - e^{-\left(\frac{t}{T'}\right)^{\beta}})$$

"M_∞" being the peak area for the longest delay spectrum and "a" a constant equal to 1 if M_∞ corresponds to the fully relaxed signal [73,74].

While spin diffusion commonly induces relaxation of all spins at a same rate (β=1), our data is best fitted for β fixed at 0.5 (Figure SI3) which is typical for relaxation dominated through space dipolar coupling with unpaired electronic spins (χ^2 is two times lower than for β=1). This result is consistent with a homogeneous iron distribution on the nanometer scale. ^{1}H T_1 relaxation also shows non-exponential behavior and relaxation curves are best fitted with a higher value of β = 0.74. Despite the fact that NMR samples have been extensively dried to remove ^{1}H from adsorbed water molecules, ^{1}H spin diffusion relaxation is still active and this value of β is typical when mixed relaxation mechanisms act on the spins [75]. As seen on Figure 3 (C,D) characteristic T' relaxation times decrease when CTAF/P123 ratio increases. This trend suggests an increase in the number of paramagnetic iron sites within the materials.

3.4. Characterization of single atom Fe@SiO_2(r) materials

A first quantitative assessment of the iron loading, obtained from both ICP-AES elementary analysis, is found to be about 0.56, 0.98, 2.31, and 2.64 wt.% for Fe@SiO_2(1), Fe@SiO_2(2), Fe@SiO_2(5), and Fe@SiO_2(10), respectively, as compared to Si (see Table 2 for the iron loading values compared to SiO_2). Those results were further confirmed by the elemental mapping obtained by scanning transmission electron microscopy (STEM). The Fe content in these materials, as compared to the Si one, is found to be about 0.8, 1.1, 2.5, and 2.7 wt.% for Fe@SiO_2(1), Fe@SiO_2(2), Fe@SiO_2(5), and Fe@SiO_2(10), respectively. Moreover, as it can be seen in Figure 4B,C and SI4, the micrographs show a homogeneous dispersion of iron atoms within the silica matrix, without formation of any agglomerates.

UV-Vis diffuse reflectance spectra (Figure SI2 right) allowed us to determine the coordination of iron in the materials. The absorption band at 235 nm, which can be assigned to the charge transfer of pπ–dπ transition between oxygen and iron in the ferrisilicate material, suggests tetrahedral iron atoms, insulated from each other. In addition, the absence of any absorbance band above 350 nm in the spectrum reveals the absence of octahedral iron ions, and consequently the absence of iron oxide nanoparticles in the Fe@SiO_2 materials [76].

The absence of nanoparticles was also confirmed by the analysis of the experimental pair distribution function derived from the corresponding total scattering measurements of the materials (Figure 4A). From the PDF diagrams, one can clearly observe well-defined features up to about 7 Å. The rapid damping of PDF oscillations beyond this distance indicates that only isolated subnanometer iron clusters might be formed and are uniformly distributed throughout the samples, with no aggregation. Larger nanoparticles would have resulted a spatial extent of atomic correlations in the PDF diagram.

It is obvious that the intensities of the PDF peaks corresponding to the contributions of the Fe atoms increase as the molar ratio r (nCTAF/nP123) increases. The first two PDF peaks located in the r range of 2.0-2.6 Å are characteristic of Fe-O distances, while the PDF peaks located in the range of 3-6 Å can be assigned to the interactions of the iron atoms with the silica pore walls or to Fe-Fe correlations.

Finally, it is noteworthy that the presence of the double peak between 2.0 and 2.6 Å indicates two related Fe environments. Further insights on the Fe oxidation, spin states and on Fe-Fe interactions were gathered from magnetic measurements.

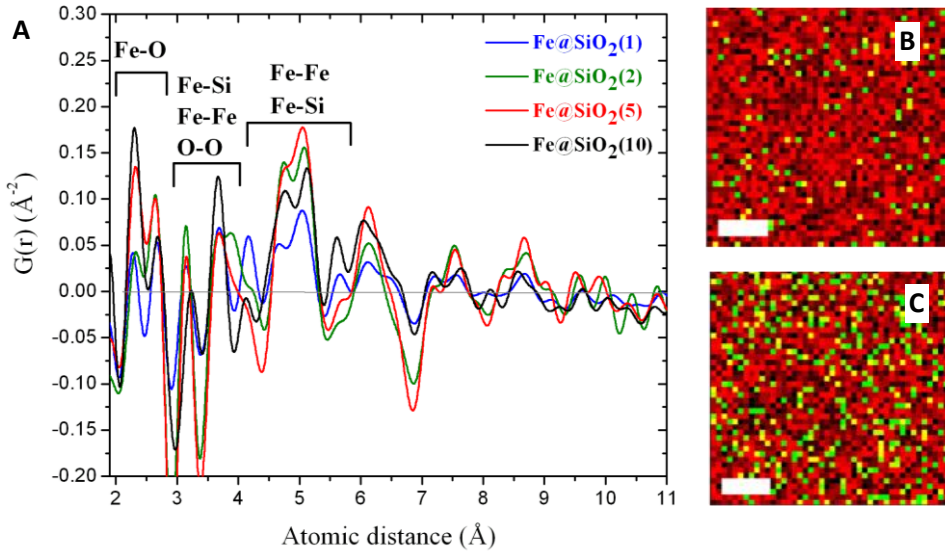

Figure 4. Comparison of experimental atomic pair distribution functions (PDFs) in real space, G(r), for Fe@SiO_2(r) materials and allocation of the main interatomic distances in the range 2 – 7 Å (A). Relative elemental maps of Fe and Si obtained by EDX in the scanning TEM mode for (B) Fe@SiO_2(1), (C) Fe@SiO_2(10) (iron in green and silica in red). The scale bare corresponds to 10 nm.

The magnetization field dependences of the Fe@SiO_2(r) measured at 10K after a first cooling at 15K·min^{-1} are plotted in Figure 5. These measurements have been subtracted from the diamagnetic contribution of sample holder and pristine P@SiO_2(r) silica, as described in SI, and have been scaled with respect to Fe content using the ICP-AES elementary analysis results. They can be fitted by a sum of two Brillouin functions as follow:

$$M(H,T) = xM_s^{5/2}B_{5/2}(H,T) + (1-x)M_s^{1/2}B_{1/2}(H,T)$$

where x is the only fitted parameter giving the proportion of the high spin S=5/2, $M_s^{5/2}$ and $M_s^{1/2}$ are the saturation magnetization of Fe^{3+} in the high spin and low spin states, respectively ($M_s^{5/2} = 500\ emu/gFe$ and $M_s^{1/2} = 100\ emu/gFe$), and $B_s(H,T)$ are the corresponding Brillouin functions (S=5/2, 1/2).

$$B_s(\alpha) = \frac{2S+1}{2S}\coth\frac{(2S+1)\alpha}{2S} - \frac{1}{2S}\coth\frac{\alpha}{2S}$$

where $\alpha = \frac{\mu_B H}{k_B T}$.

The fit with the aforementioned $M(H,T)$ equation has been performed for samples exhibiting a Curie temperature dependence under 79.6 kA/m above 10K (see Figure SI5).

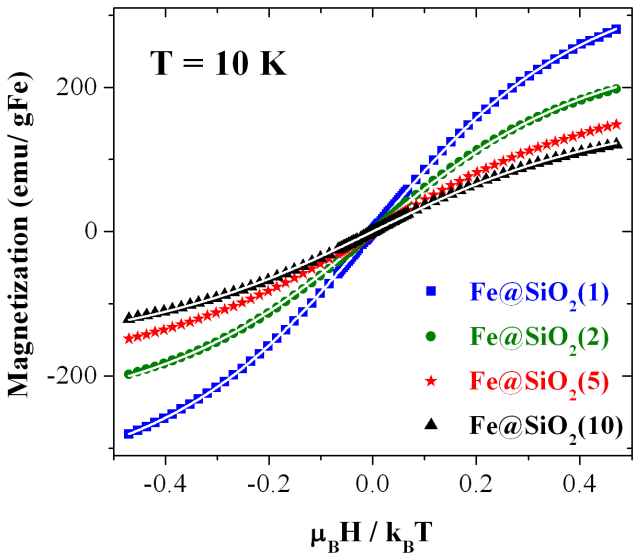

Figure 5. Field dependence behavior of the magnetization measured at 10K and corrected from the diamagnetic signal for Fe@SiO_2(r) (r = 1, 2, 5, 10) samples. It is plotted as a function of the dimensionless parameter $\mu_B H / k_B T$ where μ_B is the Bohr magneton and k_B the Boltzmann constant. The straight lines are fits by the sum of the two Brillouin functions corresponding to S = 5/2 and 1/2.

Despite only one parameter is fitted, a very good agreement is obtained between the simple model and the measurements. The fit is not changing while taking into account an additional contribution of Fe^{2+} (S=2), confirming thus the presence of solely Fe^{3+} ions. No ferromagnetic contribution is detectable at this scale. The high spin fractions deduced from the fits are reported in Table 2. They are in good agreement with those deduced from the Curie constant (see Figure SI5). No fit with the Brillouin equation has been performed for the Fe@SiO_2(5) sample since the temperature dependence of the magnetization deviates from the Curie law below 15 K (see figure SI6). This deviation is attributed to spin crossover towards low spin with decreasing temperature, which occurs below 10 K for other samples (Figure SI7). Nevertheless, the high spin fraction reported in Table 2 is stable with temperature above 10 K (or 15 K for Fe@SiO_2(5)) and is then a relevant parameter characterizing the Fe sites in the silica pores. It decreases as the Fe content increases, concomitantly with the decrease of the pore size. Thus, beyond the sharing of Fe spin state according to Si sites or pore sizes, the consistent quantitative analysis in terms of Curie law or Brillouin function without interaction between Fe spins (no Curie-Weiss temperature) supports the assumption of isolated Fe atomic centers that are well dispersed within the materials.

Table 2. Fe content (wt.%) with respect to the total samples mass used to scale the magnetization. Fraction of Fe^{3+} spins in the high spin state (5/2) deduced from the temperature dependence of magnetization (Curie law) or field dependence of magnetization measured at 10 K.

	Fe loading (wt.%)	$x_{5/2}^{Curie}$	$x_{5/2}^{Brillou}$
Fe@SiO_2(1)	0.23	0.72	0.71
Fe@SiO_2(2)	0.41	0.49	0.47
Fe@SiO_2(5)	0.97	0.31*	-
Fe@SiO_2(10)	1.08	0.25	0.24

*No fit with Brillouin functions has been performed for Fe@SiO_2(5) as it deviates from the Curie law below 15K. For this sample, the fit with the Curie law has been performed in the 15-30 K.

3.5. DFT calculations

Several structural configurations of the Fe/SiO_2 system were calculated in order to determine the most favorable adsorption position (top *vs* bridge, Figure 6) as well as the spin state, without or under geometrical constraints (2% contraction of the silica surface along the x and y directions), as in mesopores. The calculations were firstly started from reasonable estimations at various adsorption positions (top, bridge) on surfaces with various silanol densities (SiO_2-7.2, SiO_2-4.6 and SiO_2-3.3) [64,65]. For each configuration, two sets of calculations were performed for the Low-Spin (LS) and High-Spin (HS) states of iron.

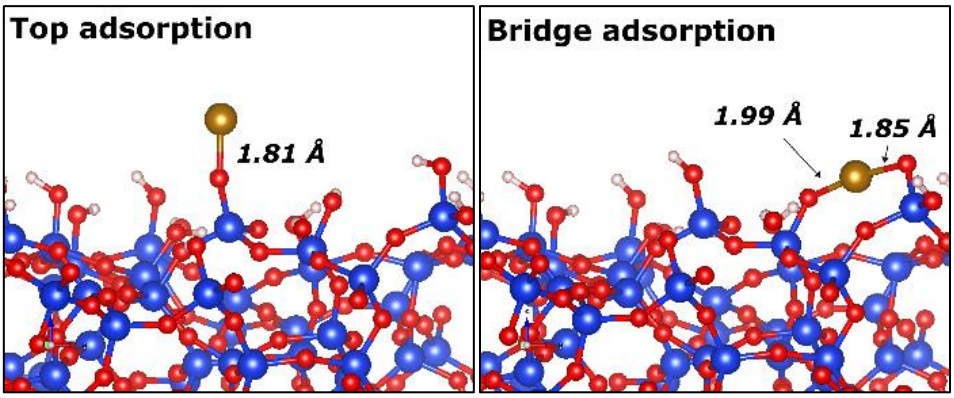

Figure 6. Panels showing the single iron atom adsorbed on amorphous silica surface with a silanol density of 4.6 OH/nm^2 at top (left) and bridge (right) positions, respectively. For the top adsorption, the equilibrium distance between the iron atom and the substrate is found to be 1.81 Å in HS and 1.78 Å in LS (left). For the bridge adsorption, in the HS state, the equilibrium iron-surface distances were found to be 1.99 and 1.85 Å for both oxygen atoms, whereas in the LS state, these distances became 1.85 and 1.81 Å, respectively (right).

The Fe atom was adsorbed on the silica surface through its oxygen atoms by removing the corresponding hydrogen atoms. Figure 6 shows the single iron atom adsorbed on the typical

488 silica surface with a silanol coverage equal to 4.6 OH per nm^2 at top (left panel) and bridge
489 (right panel) positions. For the top positions, the HS state magnetic moment of iron is 4.97 μB
490 (S =5/2) while the one of the LS state is 1.00 μB (S =1/2), which correspond to Fe^{3+}.
491 However, the HS and LS state magnetic moments of the iron in the bridge positions are found
492 to be 4.00 μB (S = 2) and 0.00 μB (S = 0), respectively, which are the HS and LS states of
493 Fe^{2+}. It is noteworthy that, for the various silica surfaces, the calculations show that the
494 adsorption of the iron atom at top positions has always the lowest total energy. Thus, the Fe^{3+}
495 oxidation state is the most favorable whatever the silanols density, in agreement with
496 experimental findings where no Fe^{2+} contribution is observed. Nevertheless, the calculations
497 show that, in the absence of geometrical constraints, the adsorption of the single iron atom on
498 various amorphous silica-surface stabilizes the HS state. This result is in contrast with
499 magnetic results where a contribution of low spins had to be considered. Such low spin state
500 is however not surprising in presence of porous materials where strains are expected.

501 Therefore, additional DFT calculations were performed starting from optimized top positions
502 at high and low spin, while taking into account geometrical constraints. The contraction of the
503 geometries along the x and y directions has been set to mimic the fact that the silica surface is
504 not perfectly planar but slightly curved which is modeled in our simulations by a pressure.
505 The choice of a contraction value of 2% has been done as a follow: the calculations with an
506 applied pressure smaller than 2% does not show a significant effect on the studied properties.
507 Also, pressures exceeding 2% are probably unrealistic and could give rise to unphysical
508 phenomena. For high silanols densities (7.2 and 4.6 OH/nm^2), our calculations (Table SI3)
509 confirm the coexistence of LS and HS Fe^{3+} species determined from magnetic measurements
510 (Table 2). For low silanols densities (3.3 OH/nm^2), the LS and HS calculations converged to
511 the same magnetic state (LS with a magnetic moment of 1 μB). This result is in line with the
512 experimental trend observed in Table 2 showing that the relative amount of LS Fe^{3+} increase
513 when decreasing the silanol density. In conclusion, DFT calculations confirmed the
514 experimental results obtained from magnetic measurements, indicating a mixture of HS and
515 LS Fe^{3+} species.

516 **4. Conclusion**

517 In this study, we demonstrated that single iron atoms-supported materials ($Fe/SiO_{2)}$ can be
518 prepared by hydrothermal synthesis using mixed non-ionic/metallosurfactants as templates.
519 The non-ionic Pluronic P123 surfactant allows controlling the structural and textural

properties of the silica framework while the ferrosurfactant acts as a metal donor, in addition to its role of porogen. The iron loading in the final materials depends on the molar ratio of surfactants and can be accurately tuned, up to 1wt% (0.15 Fe atoms/nm^2). Pair distribution function analysis, STEM mapping and magnetic measurements demonstrated the absence of any particle or cluster. Experimental data showed that the Fe species are Fe^{3+}, in agreement with the DFT calculations. Those materials proved a good distribution of iron atoms on the silica surface, with increased number of active sites, which might find straightforward applications in catalysis [2–7].

Acknowledgements

Authors would like to thank S. Parant for technical assistance with spectroscopic measurements, C. Gardiennet and G. Kervern for useful discussions on NMR. Authors acknowledge the Center of Magnetism of the Institute Jean Lamour for magnetic measurements facilities and the X-ray diffraction platform PMD²X of the Institut Jean Barriol for SAXS measurements time. The authors acknowledge financial support from the "Mirabelle+" project of the "Lorraine Université d'Excellence"(Investissements d'avenir – ANR), CPER Enerbatin and PHC CEDRE Future Materials. SG, SL and MB also acknowledge financial support through the COMETE project (COnception in silico de Matériaux pour l'EnvironnemenT et l'Energie) co-funded by the European Union under the program "FEDER-FSE Lorraine et Massif des Vosges 2014-2020". HPC resources have been provided by GENCI-CCRT (Grant and No. A0060910433).

Author Contributions

The manuscript was written through contributions of all authors.

Funding Sources

FEDER, LUE, ANR, CNRS Lebanon, Lebanese University.

Abbreviations

CTAF cetyltrimethylammoniumtrichloromonobromoferrate, DFT Density Functional Theory, STEM scanning transmission electron microscopy.

Supplementary data

1. Structural properties of pristine SBA-15-like material, obtained in the absence of CTAF; 2. Spectroscopic measurements (ATR and UV-Vis); 3. Thermogravimetric analysis; 4. NMR; 5. Elemental cartography; 6. Magnetic measurements (substraction of the diamagnetic signal and low temperature spin crossover) and 7. DFT calculations.

References

[1] M. Li, Z. Zhao, T. Cheng, A. Fortunelli, C.-Y. Chen, R. Yu, Q. Zhang, L. Gu, B.V. Merinov, Z. Lin, E. Zhu, T. Yu, Q. Jia, J. Guo, L. Zhang, W.A. Goddard, Y. Huang, X. Duan, Ultrafine jagged platinum nanowires enable ultrahigh mass activity for the oxygen reduction reaction, Science. 354 (2016) 1414–1419. https://doi.org/10.1126/science.aaf9050.

[2] P. Chen, T. Zhou, L. Xing, K. Xu, Y. Tong, H. Xie, L. Zhang, W. Yan, W. Chu, C. Wu, Y. Xie, Atomically Dispersed Iron-Nitrogen Species as Electrocatalysts for Bifunctional Oxygen Evolution and Reduction Reactions, Angew. Chem. 129 (2017) 625–629. https://doi.org/10.1002/ange.201610119.

[3] J.M. Thomas, R. Raja, The advantages and future potential of single-site heterogeneous catalysts, Top. Catal. 40 (2006) 3–17. https://doi.org/10.1007/s11244-006-0105-7.

[4] X.-F. Yang, A. Wang, B. Qiao, J. Li, J. Liu, T. Zhang, Single-Atom Catalysts: A New Frontier in Heterogeneous Catalysis, Acc. Chem. Res. 46 (2013) 1740–1748. https://doi.org/10.1021/ar300361m.

[5] A. Wang, J. Li, T. Zhang, Heterogeneous single-atom catalysis, Nat. Rev. Chem. 2 (2018) 65–81. https://doi.org/10.1038/s41570-018-0010-1.

[6] H. Zhang, G. Liu, L. Shi, J. Ye, Single-Atom Catalysts: Emerging Multifunctional Materials in Heterogeneous Catalysis, Adv. Energy Mater. 8 (2018) 1701343. https://doi.org/10.1002/aenm.201701343.

[7] Y. Chen, S. Ji, C. Chen, Q. Peng, D. Wang, Y. Li, Single-Atom Catalysts: Synthetic Strategies and Electrochemical Applications, Joule. 2 (2018) 1242–1264. https://doi.org/10.1016/j.joule.2018.06.019.

[8] J. Jones, H. Xiong, A.T. DeLaRiva, E.J. Peterson, H. Pham, S.R. Challa, G. Qi, S. Oh, M.H. Wiebenga, X.I. Pereira Hernandez, Y. Wang, A.K. Datye, Thermally stable single-atom platinum-on-ceria catalysts via atom trapping, Science. 353 (2016) 150–154. https://doi.org/10.1126/science.aaf8800.

[9] S. Sun, G. Zhang, N. Gauquelin, N. Chen, J. Zhou, S. Yang, W. Chen, X. Meng, D. Geng, M.N. Banis, R. Li, S. Ye, S. Knights, G.A. Botton, T.-K. Sham, X. Sun, Single-atom Catalysis Using Pt/Graphene Achieved through Atomic Layer Deposition, Sci. Rep. 3 (2013). https://doi.org/10.1038/srep01775.

[10] H. Yan, H. Cheng, H. Yi, Y. Lin, T. Yao, C. Wang, J. Li, S. Wei, J. Lu, Single-Atom Pd_1/Graphene Catalyst Achieved by Atomic Layer Deposition: Remarkable Performance in Selective Hydrogenation of 1,3-Butadiene, J. Am. Chem. Soc. 137 (2015) 10484–10487. https://doi.org/10.1021/jacs.5b06485.

[11] J. Lin, A. Wang, B. Qiao, X. Liu, X. Yang, X. Wang, J. Liang, J. Li, J. Liu, T. Zhang, Remarkable Performance of Ir_1/FeO_x Single-Atom Catalyst in Water Gas Shift Reaction, J. Am. Chem. Soc. 135 (2013) 15314–15317. https://doi.org/10.1021/ja408574m.

[12] B. Qiao, L. Liu, J. Zhang, Y. Deng, Preparation of highly effective ferric hydroxide supported noble metal catalysts for CO oxidations: From gold to palladium, J. Catal. 261 (2009) 241–244. https://doi.org/10.1016/j.jcat.2008.11.012.
[13] B. Qiao, A. Wang, X. Yang, L.F. Allard, Z. Jiang, Y. Cui, J. Liu, J. Li, T. Zhang, Single-atom catalysis of CO oxidation using Pt_1/FeO_x, Nat. Chem. 3 (2011) 634–641. https://doi.org/10.1038/nchem.1095.
[14] F. Li, Y. Li, X.C. Zeng, Z. Chen, Exploration of High-Performance Single-Atom Catalysts on Support M_1/FeO_x for CO Oxidation via Computational Study, ACS Catal. 5 (2015) 544–552. https://doi.org/10.1021/cs501790v.
[15] B. Qiao, J.-X. Liang, A. Wang, C.-Q. Xu, J. Li, T. Zhang, J.J. Liu, Ultrastable single-atom gold catalysts with strong covalent metal-support interaction (CMSI), Nano Res. 8 (2015) 2913–2924. https://doi.org/10.1007/s12274-015-0796-9.
[16] B. Qiao, J. Liu, Y.-G. Wang, Q. Lin, X. Liu, A. Wang, J. Li, T. Zhang, J. (Jimmy) Liu, Highly Efficient Catalysis of Preferential Oxidation of CO in H_2-Rich Stream by Gold Single-Atom Catalysts, ACS Catal. 5 (2015) 6249–6254. https://doi.org/10.1021/acscatal.5b01114.
[17] P. Liu, Y. Zhao, R. Qin, S. Mo, G. Chen, L. Gu, D.M. Chevrier, P. Zhang, Q. Guo, D. Zang, B. Wu, G. Fu, N. Zheng, Photochemical route for synthesizing atomically dispersed palladium catalysts, Science. 352 (2016) 797–800. https://doi.org/10.1126/science.aaf5251.
[18] P. Yin, T. Yao, Y. Wu, L. Zheng, Y. Lin, W. Liu, H. Ju, J. Zhu, X. Hong, Z. Deng, G. Zhou, S. Wei, Y. Li, Single Cobalt Atoms with Precise N-Coordination as Superior Oxygen Reduction Reaction Catalysts, Angew. Chem. 128 (2016) 10958–10963. https://doi.org/10.1002/ange.201604802.
[19] Y. Chen, S. Ji, Y. Wang, J. Dong, W. Chen, Z. Li, R. Shen, L. Zheng, Z. Zhuang, D. Wang, Y. Li, Isolated Single Iron Atoms Anchored on N-Doped Porous Carbon as an Efficient Electrocatalyst for the Oxygen Reduction Reaction, Angew. Chem. 129 (2017) 7041–7045. https://doi.org/10.1002/ange.201702473.
[20] L. Yang, D. Cheng, H. Xu, X. Zeng, X. Wan, J. Shui, Z. Xiang, D. Cao, Unveiling the high-activity origin of single-atom iron catalysts for oxygen reduction reaction, Proc. Natl. Acad. Sci. 115 (2018) 6626–6631. https://doi.org/10.1073/pnas.1800771115.
[21] H. Fei, J. Dong, Y. Feng, C.S. Allen, C. Wan, B. Volosskiy, M. Li, Z. Zhao, Y. Wang, H. Sun, P. An, W. Chen, Z. Guo, C. Lee, D. Chen, I. Shakir, M. Liu, T. Hu, Y. Li, A.I. Kirkland, X. Duan, Y. Huang, General synthesis and definitive structural identification of MN4C4 single-atom catalysts with tunable electrocatalytic activities, Nat. Catal. 1 (2018) 63–72. https://doi.org/10.1038/s41929-017-0008-y.
[22] S. Back, J. Lim, N.-Y. Kim, Y.-H. Kim, Y. Jung, Single-atom catalysts for CO_2 electroreduction with significant activity and selectivity improvements, Chem. Sci. 8 (2017) 1090–1096. https://doi.org/10.1039/C6SC03911A.
[23] M. Flytzani-Stephanopoulos, B.C. Gates, Atomically Dispersed Supported Metal Catalysts, Annu. Rev. Chem. Biomol. Eng. 3 (2012) 545–574. https://doi.org/10.1146/annurev-chembioeng-062011-080939.
[24] C. Nozaki, C.G. Lugmair, A.T. Bell, T.D. Tilley, Synthesis, Characterization, and Catalytic Performance of Single-Site Iron(III) Centers on the Surface of SBA-15 Silica, J. Am. Chem. Soc. 124 (2002) 13194–13203. https://doi.org/10.1021/ja020388t.
[25] B. Hu, N.M. Schweitzer, G. Zhang, S.J. Kraft, D.J. Childers, M.P. Lanci, J.T. Miller, A.S. Hock, Isolated Fe^{II} on Silica As a Selective Propane Dehydrogenation Catalyst, ACS Catal. 5 (2015) 3494–3503. https://doi.org/10.1021/acscatal.5b00248.

[26] R.N. Olcese, M. Bettahar, D. Petitjean, B. Malaman, F. Giovanella, A. Dufour, Gas-phase hydrodeoxygenation of guaiacol over Fe/SiO_2 catalyst, Appl. Catal. B Environ. 115–116 (2012) 63–73. https://doi.org/10.1016/j.apcatb.2011.12.005.
[27] N. Wang, W. Chu, T. Zhang, X.S. Zhao, Synthesis, characterization and catalytic performances of Ce-SBA-15 supported nickel catalysts for methane dry reforming to hydrogen and syngas, Int. J. Hydrog. Energy. 37 (2012) 19–30. https://doi.org/10.1016/j.ijhydene.2011.03.138.
[28] D.J. Kim, B.C. Dunn, F. Huggins, G.P. Huffman, M. Kang, J.E. Yie, E.M. Eyring, SBA-15-Supported Iron Catalysts for Fischer−Tropsch Production of Diesel Fuel, Energy Fuels. 20 (2006) 2608–2611. https://doi.org/10.1021/ef060336f.
[29] G. Prieto, A. Martínez, R. Murciano, M.A. Arribas, Cobalt supported on morphologically tailored SBA-15 mesostructures: The impact of pore length on metal dispersion and catalytic activity in the Fischer–Tropsch synthesis, Appl. Catal. Gen. 367 (2009) 146–156. https://doi.org/10.1016/j.apcata.2009.08.003.
[30] L.A. Cano, M.V. Cagnoli, J.F. Bengoa, A.M. Alvarez, S.G. Marchetti, Effect of the activation atmosphere on the activity of Fe catalysts supported on SBA-15 in the Fischer–Tropsch Synthesis, J. Catal. 278 (2011) 310–320. https://doi.org/10.1016/j.jcat.2010.12.017.
[31] Y. Sun, S. Walspurger, J.-P. Tessonnier, B. Louis, J. Sommer, Highly dispersed iron oxide nanoclusters supported on ordered mesoporous SBA-15: A very active catalyst for Friedel–Crafts alkylations, Appl. Catal. Gen. 300 (2006) 1–7. https://doi.org/10.1016/j.apcata.2005.10.029.
[32] B. Karimi, S. Abedi, J.H. Clark, V. Budarin, Highly Efficient Aerobic Oxidation of Alcohols Using a Recoverable Catalyst: The Role of Mesoporous Channels of SBA-15 in Stabilizing Palladium Nanoparticles, Angew. Chem. Int. Ed. 45 (2006) 4776–4779. https://doi.org/10.1002/anie.200504359.
[33] X. Liu, A. Wang, X. Wang, C.-Y. Mou, T. Zhang, Au–Cu Alloy nanoparticles confined in SBA-15 as a highly efficient catalyst for CO oxidation, Chem. Commun. (2008) 3187. https://doi.org/10.1039/b804362k.
[34] F. Rajabi, S. Naserian, A. Primo, R. Luque, Efficient and Highly Selective Aqueous Oxidation of Sulfides to Sulfoxides at Room Temperature Catalysed by Supported Iron Oxide Nanoparticles on SBA-15, Adv. Synth. Catal. 353 (2011) 2060–2066. https://doi.org/10.1002/adsc.201100149.
[35] H. Huang, Y. Ji, Z. Qiao, C. Zhao, J. He, H. Zhang, Preparation, Characterization, and Application of Magnetic Fe-SBA-15 Mesoporous Silica Molecular Sieves, J. Autom. Methods Manag. Chem. 2010 (2010) 323509. https://doi.org/10.1155/2010/323509.
[36] Y. Li, Z. Feng, Y. Lian, K. Sun, L. Zhang, G. Jia, Q. Yang, C. Li, Direct synthesis of highly ordered Fe-SBA-15 mesoporous materials under weak acidic conditions, Microporous Mesoporous Mater. 84 (2005) 41–49. https://doi.org/10.1016/j.micromeso.2005.05.021.
[37] J.M. Campelo, D. Luna, R. Luque, J.M. Marinas, A.A. Romero, Sustainable Preparation of Supported Metal Nanoparticles and Their Applications in Catalysis, ChemSusChem. 2 (2009) 18–45. https://doi.org/10.1002/cssc.200800227.
[38] A. Barau, V. Budarin, A. Caragheorgheopol, R. Luque, D.J. Macquarrie, A. Prelle, V.S. Teodorescu, M. Zaharescu, A Simple and Efficient Route to Active and Dispersed Silica Supported Palladium Nanoparticles, Catal. Lett. 124 (2008) 204–214. https://doi.org/10.1007/s10562-008-9465-x.
[39] N.C. King, R.A. Blackley, W. Zhou, D.W. Bruce, The preparation by true liquid crystal templating of mesoporous silicates containing nanoparticulate metals, Chem. Commun. (2006) 3411. https://doi.org/10.1039/b607470g.

[40] N.C. King, R.A. Blackley, M.L. Wears, D.M. Newman, W. Zhou, D.W. Bruce, The synthesis of mesoporous silicates containing bimetallic nanoparticles and magnetic properties of PtCo nanoparticles in silica, Chem. Commun. (2006) 3414. https://doi.org/10.1039/b607471e.
[41] H. Liu, D. Ma, R.A. Blackley, W. Zhou, X. Bao, Highly active mesostructured silica hosted silver catalysts for CO oxidation using the one-pot synthesis approach, Chem. Commun. (2008) 2677. https://doi.org/10.1039/b804641g.
[42] S. Kim, C. Bellouard, A. Pasc, E. Lamouroux, J.-L. Blin, C. Carteret, Y. Fort, M. Emo, P. Durand, M.-J. Stébé, Nanoparticle-free magnetic mesoporous silica with magneto-responsive surfactants, J. Mater. Chem. C. 1 (2013) 6930–6934. https://doi.org/10.1039/C3TC31617C.
[43] S. Kim, C. Bellouard, J. Eastoe, N. Canilho, S.E. Rogers, D. Ihiawakrim, O. Ersen, A. Pasc, Spin State As a Probe of Vesicle Self-Assembly, J. Am. Chem. Soc. 138 (2016) 2552–2555. https://doi.org/10.1021/jacs.6b00537.
[44] S. Kim, P. Durand, T. Roques-Carmes, J. Eastoe, A. Pasc, Metallo-Solid Lipid Nanoparticles as Colloidal Tools for Meso–Macroporous Supported Catalysts, Langmuir. 31 (2015) 1842–1849. https://doi.org/10.1021/la504708k.
[45] S. Brunauer, P.H. Emmett, E. Teller, Adsorption of Gases in Multimolecular Layers, J. Am. Chem. Soc. 60 (1938) 309–319. https://doi.org/10.1021/ja01269a023.
[46] F. Rouquerol, J. Rouquerol, K.S.W. Sing, Adsorption by powders and porous solids: principles, methodology, and applications, Academic Press, San Diego, 1999.
[47] P. Tarazona, U.M.B. Marconi, R. Evans, Phase equilibria of fluid interfaces and confined fluids: Non-local versus local density functionals, Mol. Phys. 60 (1987) 573–595. https://doi.org/10.1080/00268978700100381.
[48] M. Kruk, M. Jaroniec, A. Sayari, Application of Large Pore MCM-41 Molecular Sieves To Improve Pore Size Analysis Using Nitrogen Adsorption Measurements, Langmuir. 13 (1997) 6267–6273. https://doi.org/10.1021/la970776m.
[49] M. Kruk, M. Jaroniec, C.H. Ko, R. Ryoo, Characterization of the Porous Structure of SBA-15, Chem. Mater. 12 (2000) 1961–1968. https://doi.org/10.1021/cm000164e.
[50] J. Kieffer, D. Karkoulis, PyFAI, a versatile library for azimuthal regrouping, J. Phys. Conf. Ser. 425 (2013) 202012. https://doi.org/10.1088/1742-6596/425/20/202012.
[51] P. Juhás, T. Davis, C.L. Farrow, S.J.L. Billinge, *PDFgetX3*: a rapid and highly automatable program for processing powder diffraction data into total scattering pair distribution functions, J. Appl. Crystallogr. 46 (2013) 560–566. https://doi.org/10.1107/S0021889813005190.
[52] K.-Y. Hsieh, E.-E. Bendeif, A. Gansmuller, S. Pillet, T. Woike, D. Schaniel, Structure and dynamics of guest molecules confined in a mesoporous silica matrix: Complementary NMR and PDF characterisation, RSC Adv. 3 (2013) 26132. https://doi.org/10.1039/c3ra45347b.
[53] E.-E. Bendeif, A. Gansmuller, K.-Y. Hsieh, S. Pillet, Th. Woike, M. Zobel, R.B. Neder, M. Bouazaoui, H. El Hamzaoui, D. Schaniel, Structure determination of molecular nanocomposites by combining pair distribution function analysis and solid-state NMR, RSC Adv. 5 (2015) 8895–8902. https://doi.org/10.1039/C4RA11470A.
[54] B.M. Fung, A.K. Khitrin, K. Ermolaev, An Improved Broadband Decoupling Sequence for Liquid Crystals and Solids, J. Magn. Reson. 142 (2000) 97–101. https://doi.org/10.1006/jmre.1999.1896.
[55] D. Massiot, F. Fayon, M. Capron, I. King, S. Le Calvé, B. Alonso, J.-O. Durand, B. Bujoli, Z. Gan, G. Hoatson, Modelling one- and two-dimensional solid-state NMR spectra: Modelling 1D and 2D solid-state NMR spectra, Magn. Reson. Chem. 40 (2002) 70–76. https://doi.org/10.1002/mrc.984.

[56] G. Kresse, J. Furthmüller, Efficient iterative schemes for *ab initio* total-energy calculations using a plane-wave basis set, Phys. Rev. B. 54 (1996) 11169–11186. https://doi.org/10.1103/PhysRevB.54.11169.
[57] P.E. Blöchl, Projector augmented-wave method, Phys. Rev. B. 50 (1994) 17953–17979. https://doi.org/10.1103/PhysRevB.50.17953.
[58] J.P. Perdew, K. Burke, M. Ernzerhof, Generalized Gradient Approximation Made Simple, Phys. Rev. Lett. 77 (1996) 3865–3868. https://doi.org/10.1103/PhysRevLett.77.3865.
[59] V.I. Anisimov, F. Aryasetiawan, A.I. Lichtenstein, First-principles calculations of the electronic structure and spectra of strongly correlated systems: the **LDA** + *U* method, J. Phys. Condens. Matter. 9 (1997) 767–808. https://doi.org/10.1088/0953-8984/9/4/002.
[60] O. Bengone, M. Alouani, P. Blöchl, J. Hugel, Implementation of the projector augmented-wave LDA+U method: Application to the electronic structure of NiO, Phys. Rev. B. 62 (2000) 16392–16401. https://doi.org/10.1103/PhysRevB.62.16392.
[61] S. Gueddida, M. Alouani, Calculated impact of ferromagnetic substrate on the spin crossover in a $Fe(1,10-phenanthroline)_2(NCS)_2$ molecule, Phys. Rev. B. 93 (2016). https://doi.org/10.1103/PhysRevB.93.184433.
[62] S. Grimme, Semiempirical GGA-type density functional constructed with a long-range dispersion correction, J. Comput. Chem. 27 (2006) 1787–1799. https://doi.org/10.1002/jcc.20495.
[63] T. Bučko, J. Hafner, S. Lebègue, J.G. Ángyán, Improved Description of the Structure of Molecular and Layered Crystals: Ab Initio DFT Calculations with van der Waals Corrections, J. Phys. Chem. A. 114 (2010) 11814–11824. https://doi.org/10.1021/jp106469x.
[64] A. Comas-Vives, Amorphous SiO_2 surface models: energetics of the dehydroxylation process, strain, ab initio atomistic thermodynamics and IR spectroscopic signatures, Phys. Chem. Chem. Phys. 18 (2016) 7475–7482. https://doi.org/10.1039/C6CP00602G.
[65] Y. Berro, S. Gueddida, S. Lebègue, A. Pasc, N. Canilho, M. Kassir, F.E.H. Hassan, M. Badawi, Atomistic description of phenol, CO and H_2O adsorption over crystalline and amorphous silica surfaces for hydrodeoxygenation applications, Appl. Surf. Sci. 494 (2019) 721–730. https://doi.org/10.1016/j.apsusc.2019.07.216.
[66] D. Zhao, Triblock Copolymer Syntheses of Mesoporous Silica with Periodic 50 to 300 Angstrom Pores, Science. 279 (1998) 548–552. https://doi.org/10.1126/science.279.5350.548.
[67] D. Zhao, J. Sun, Q. Li, G.D. Stucky, Morphological Control of Highly Ordered Mesoporous Silica SBA-15, Chem. Mater. 12 (2000) 275–279. https://doi.org/10.1021/cm9911363.
[68] V.I. Bakhmutov, Strategies for Solid-State NMR Studies of Materials: From Diamagnetic to Paramagnetic Porous Solids, Chem. Rev. 111 (2011) 530–562. https://doi.org/10.1021/cr100144r.
[69] H.-I. Kim, S.K. Lee, The degree of polymerization and structural disorder in (Mg,Fe)SiO3 glasses and melts: Insights from high-resolution ^{29}Si and ^{17}O solid-state NMR, Geochim. Cosmochim. Acta. 250 (2019) 268–291. https://doi.org/10.1016/j.gca.2019.02.018.
[70] M.J. Duer, ed., Solid-state NMR spectroscopy: principles and applications, Blackwell Science, Malden, MA, 2002.
[71] R.M. Hazen, L.W. Finger, High-pressure crystal chemistry of andradite and pyrope; revised procedures for high-pressure diffraction experiments, Am. Mineral. 74 (1989) 352–359.

[72] T. Armbruster, C.A. Geiger, G.A. Lager, Single-crystal X-ray structure study of synthetic pyrope almandine garnets at 100 and 293 K, Am. Mineral. 77 (1992) 512–521.
[73] D. Tse, S.R. Hartmann, Nuclear Spin-Lattice Relaxation Via Paramagnetic Centers Without Spin Diffusion, Phys. Rev. Lett. 21 (1968) 511–514. https://doi.org/10.1103/PhysRevLett.21.511.
[74] J.S. Hartman, B.L. Sherriff, Silicon-29 MAS NMR of the aluminosilicate mineral kyanite: residual dipolar coupling to aluminum-27 and nonexponential spin-lattice relaxation, J. Phys. Chem. 95 (1991) 7575–7579. https://doi.org/10.1021/j100173a005.
[75] J.S. Hartman, A. Narayanan, S.S. Rigby, D.R. Sliwinski, N.M. Halden, A.D. Bain, Heterogeneities in sol–gel-derived paramagnetics-doped forsterites and willemites — Electron microprobe analysis and stretched-exponential ^{29}Si MAS NMR spin–lattice relaxation studies, Can. J. Chem. 85 (2007) 56–65. https://doi.org/10.1139/v06-183.
[76] B. Li, J. Xu, J. Liu, S. Zuo, Z. Pan, Z. Wu, Preparation of mesoporous ferrisilicate with high content of framework iron by pH-modification method and its catalytic performance, J. Colloid Interface Sci. 366 (2012) 114–119. https://doi.org/10.1016/j.jcis.2011.09.055.